

**Hot Electron and Pair Production from the Texas Petawatt Laser  
Irradiating Thick Gold Targets**

Devin Taylor, Edison Liang, Taylor Clark, Alexander Henderson, Petr Shagin, Xin Wang  
Rice University

and

Gilliss Dyer, Kristina Serratto, Nathan Riley, Michael Donovan, Todd Ditmire,  
University of Texas at Austin

**Abstract**

We present data from electron-positron pair production by an ultra-intense laser incident on solid Au targets with thickness between 1 and 4 mm. The experiment was performed at the Texas Petawatt Laser in July 2011, with intensities on the order of several  $\times 10^{19} \text{ W.cm}^{-2}$  and laser energies around 50 J. We discuss the design of an electron-positron magnetic spectrometer to record the lepton energy spectra ejected from the Au targets. We then present a deconvolution algorithm to extract the lepton energy spectra. We measured hot electron spectra out to  $> 50 \text{ MeV}$ , which show a narrow peak around 10 – 15 MeV, plus exponential tail consistent with ponderomotive temperature scaling. We did not observe direct evidence of positron production above the background, even though separate gamma-ray measurement hints at the presence of positrons.

## Chapter 1 Introduction

The study of electron-positron pair plasmas is believed to be prominent in many high-energy astrophysical processes including gamma-ray bursts, blazer jets, and pulsar winds. Recently, short-pulse lasers have advanced enough to allow these processes to be studied in the laboratory. These ultra-intense lasers can be utilized to produce many electron-positron pairs in the multi-MeV range.[7]

### 1.1 Hot Electron and Pair Production

When an ultra-intense laser strikes a solid target, superthermal electrons are produced with characteristic energy approximated by [1, 9]

$$E_{\text{hot}} = [(1 + I \lambda^2 / 1.4 \times 10^{18})^{1/2} - 1] mc^2$$

where  $I$  is the laser intensity in  $\text{W.cm}^{-2}$  and  $\lambda$  is the laser wavelength in microns. If the incident laser intensity is great enough (so that  $E_{\text{hot}} > 2mc^2$ ), these hot electrons will then pair produce inside a high-Z target.

The process of electron-positron pair production from electrons interacting with a nucleus can occur through two channels, the Trident process or the Bethe-Heitler process [1, 3]. The Trident process is the process by which electrons produce pairs by directly interacting with the nucleus. This process dominates for thin foils. We are using thick targets in our experiment, and thus the Bethe-Heitler [10] process will dominate. This process proceeds through the creation of bremsstrahlung photons which then interact with the nuclei to form an electron-positron pair [3].

When the incident, photoelectric and Compton scattered electrons exit the target, they form a sheath electric field that then accelerates the positrons once they leave the target. The sheath electric field forms on the order of a few tens of femtoseconds and can be very intense for high-Z targets. Hence the majority of positrons may travel through this field, gaining energy equal to the potential of the field. This then shifts the peak energy of the resultant positron energy spectrum up by several MeV. This field also causes the positrons to form a jet out of the back of the target. The positron energy and density are thus greater along the target normal axis along the back of the target, and there is a dearth perpendicular to this axis [3].

### 1.2 Texas Petawatt Laser

The experiment was conducted at the Texas Petawatt Laser operated from the University of Texas at Austin campus. The laser is based on an optical parametric chirped pulse amplification (OPCPA) design with mixed silicate and phosphorus Nd:glass amplification. Such a design allows a shorter pulse duration and thus higher intensity on target [6]. The design specifications of the laser give an estimated maximum energy on target of up to 200 J with a pulse duration of 150fs and spot size of 5 m.[6] Using the equation for laser intensity

$$I = P_p / A ; P_p = E / \Delta t$$

where  $P_p$  is peak power,  $A$  is the area of the spot incident on the laser target,  $E$  is energy, and  $\Delta t$  is the pulse duration, we expect a peak intensity  $I$  of  $> 10^{21} \text{W/cm}^2$ . However, during our experimental run, the laser was not operating at maximum energy to avoid damage to the focusing optics. Thus, we saw an energy range of 40 – 50 J and a longer pulse duration on the order of 200 – 400 fs and in turn saw a maximum intensity of only several  $10^{19} \text{W/cm}^2$ .

## Chapter 2 Experimental Design

The goal of the experiment is to measure electron and positron production from an ultra-intense laser incident on a high-Z solid target. The solid targets are chosen to be Au ( $Z = 79$ ) because of its high-Z and high density. Such high-Z material allows for a greater ratio of electron-positron pair production to electrons generated from Compton scattering. Targets of various thicknesses are fabricated from 1- 4 mm. The targets are not thin enough to have significant electron-positron production through the Trident process, which occurs for thin targets below 30 microns [3]. We are interested in examining electron and positron generation through the Bethe-Heitler process [10] that dominates with thick targets.

To determine the number and spectra of produced electrons and positrons, a magnetic spectrometer is designed and fabricated as the principle diagnostics device. Secondary confirmation of positron production is accomplished via gamma ray spectrometers. The magnetic spectrometer was placed in the target normal position as indicated in Figure 2.1. This position is chosen because of its use in previous literature. Through Monte Carlo simulation, it is determined that the peak positron production will occur at a point between the target normal direction and laser forward direction. Future studies will see the spectrometer moved to this position. The spectrometer's designed energy range is 1-50 MeV. To complement this high energy spectrometer, a low energy weak-field spectrometer is borrowed from UT-Austin to cover the range  $< 6 \text{ MeV}$ .

The data recording mechanism is chosen to be phosphorus image plates. These plates offer the benefit of a quick read time without complicated electronics inside the chamber. However, the data is wiped by visible light and degrades over time, therefore the image plates must be digitally recorded within 90 minutes or risk data loss. The specifications of these image plates are discussed in detail in the next section. We were assigned 1 week of shot time and carried out 14 shots.

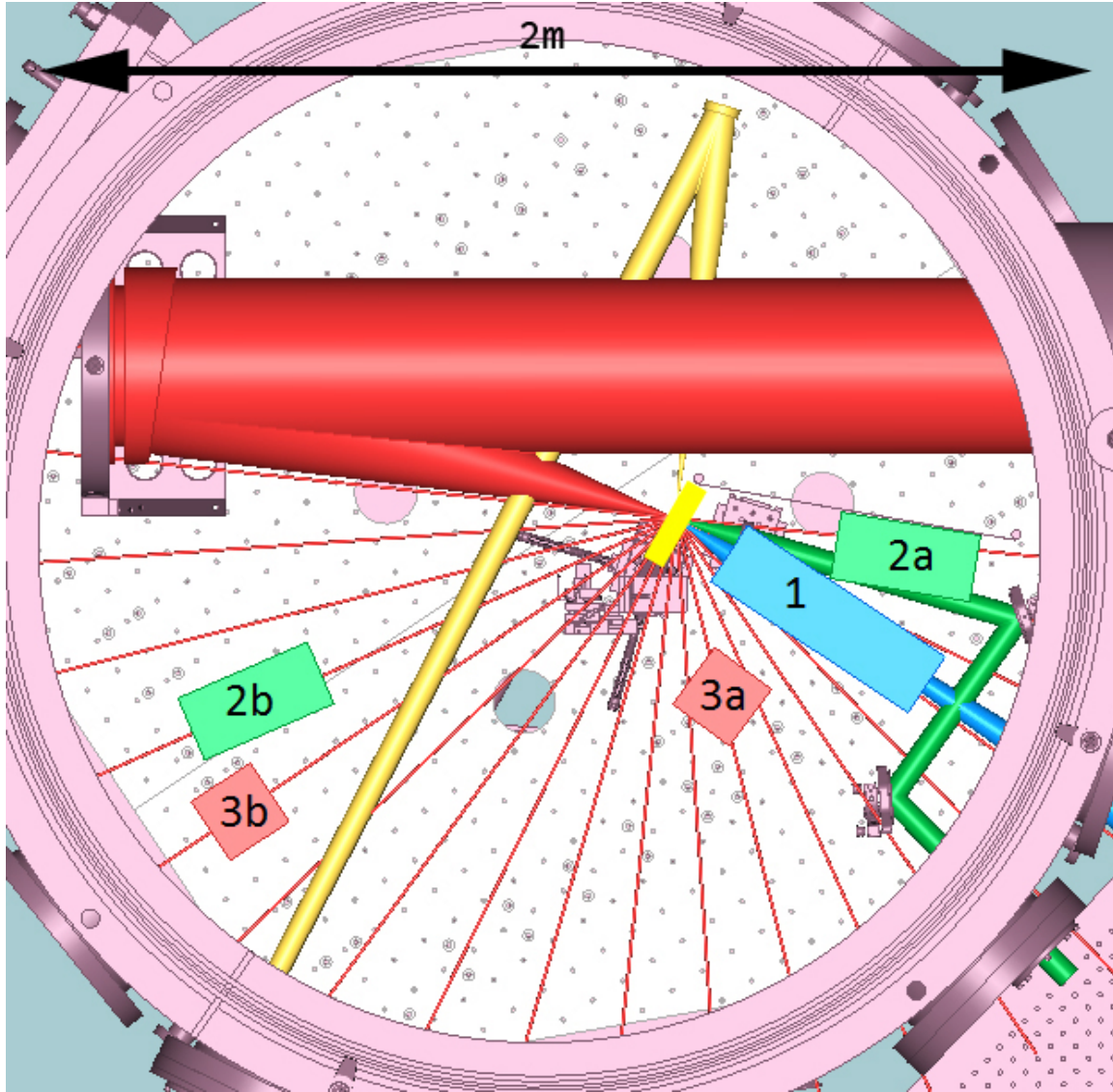


Figure 2.1: The target chamber set-up for the TPW experimental run in July 2011 (the red lines are in 10 degree increments about laser forward direction). The yellow box indicates the orientation of our targets at 17 degrees from laser forward. (1) The high energy spectrometer was placed at a variable distance of 9-22 cm at target normal. (2) The low energy spectrometer was first placed at (a) 4 degrees outside laser forward and later placed at (b) the front of the target. (3) The gamma ray spectrometers: (a) looking at the high energy spectrometer positron side and (b) various other locations looking directly at the target.

### Chapter 3 Spectrometer

The principle work over the spring and summer of 2011 involved the design and fabrication of the magnetic electron-positron spectrometer. Previous work determined the magnetic field necessary to give the desired energy range must be 0.6T. Past experiments working with electron production from ultra-intense lasers have had good success with the use of phosphorus image plates (BAS SR2040)[3]. The plates do not require development and are thus reusable. In addition, the image plates can be read quickly via an image plate scanner and their response to deposited electrons has been well studied [2, 5]. However, the image plates are sensitive to x-

rays. Hence, a major element of the design effort is the reduction of the x-ray background via shielding.

### 3.1 Design

The spectrometer's design consists of three components: the outer case, the inner spectrometer, and the shielding. Because the response of the spectrometer could not be determined prior to the experimental run beyond Monte Carlo simulation, the spectrometer is designed to be adaptable. The outer spectrometer case is designed to be semi-light tight. This is necessary because the image plates used in the spectrometer are wiped by visible light.

The inner spectrometer consists of two neodymium-iron-boride (Nd-Fe-B) magnets separated by a distance of 1.4 cm to achieve peak magnetic field strength of approximately 0.6T in the gap. The orientation of the field is such that the positrons will travel to the right and electrons will travel to the left when viewed from the top. The magnets are separated by Fe yokes that are intended to contain the magnetic field. In this way, the electrons will not be significantly diverted from the central axis until they are within the inner spectrometer. This would ideally increase the lower energy resolution of the spectrometer. As a side effect of the Fe yokes, the spectrometer gains a new background source from fluorescence of the Fe yoke. Because of the fringe magnetic fields at the magnet edges, electrons tend to be focused towards the mid-plane of the gap.

Because the image plates are slightly magnetic, it is not necessary to design a complex fastening mechanism for the plates. A thin cavity is etched into the Al siding of the spectrometer to hold the image plates. The plates are cut to 1in by 6in and placed such that the plate runs the length of the magnet. The Fe yokes provide a clearly visible line to indicate the beginning of the spectrometer. The shielding is expandable with the ability to have arbitrary thickness up to a maximum of approximately 4in. The configuration determined to be most suitable is alternating layers of 0.5 in Pb and Cu with a total thickness of 2in. Through the shielding, a 3mm collimating pinhole is bored. Shielding with a 2mm collimating pinhole is also available if it is determined that the signal must be reduced.



Figure 3.1 Magnetic spectrometer with Al case and 3 mm pinhole. The outer case dimensions are 3.5 inches x 4.5 inches x 12 inches. It can measure  $e^+e^-$  energies from  $\sim 1$  MeV – 55 MeV.

### 3.2 Calibration

Calibration of the spectrometer must be done for the low and high energy spectrum. The low energy calibration can be accomplished with a standard radioactive source.  $^{90}\text{Sr}$  is chosen because the emitted electron energy range edge is relatively high at 2.28 MeV. To get the higher energy calibration, it is necessary to go to an electron beam line. We used the LSU MBPCC beam line, which has an adjustable energy range of  $\sim 6 - 20$  MeV, allowing multiple upper energy calibration points.

The  $^{90}\text{Sr}$  radioactive source undergoes two beta decays with two distinct energy range edges at 0.546 MeV and 2.28 MeV.



The lowest energy is not visible in our spectrometer, which has an energy range of 1 – 50 MeV. The electron beam line at LSU is an Elekta radiotherapy linear accelerator capable of producing mono-energetic electrons in the energy range of 6-22 MeV. Several data points were taken with different beam energies to verify the Monte Carlo simulated energy spectrum based on the 3-D measured B-field map. The LSU electron beam data and the simulated position data are found to agree to better than  $< 1$  mm [8]. With such close agreement, the simulated point spread functions are taken to be good approximations of the true spectrometer point spread functions and are thus used in the deconvolution algorithm.

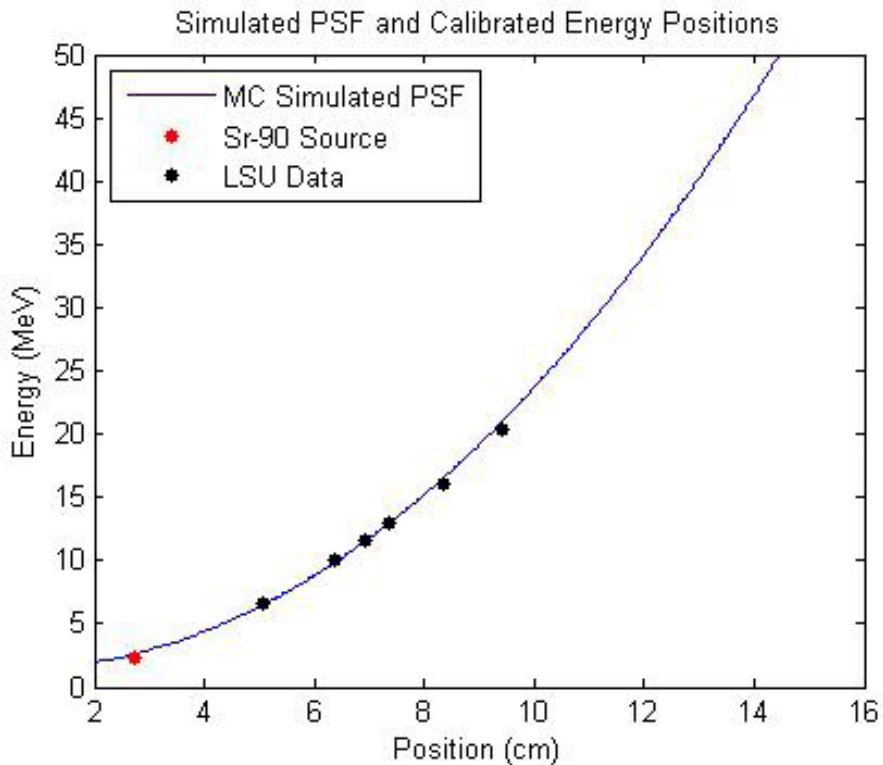


Figure 3.2: Calibrated electron energy spectrum from LSU data points [8] and  $^{90}\text{Sr}$  source.

## Chapter 4 Data Analysis

The primary work of this year has been the analysis of the data generated by the 2011 summer run at the Texas Petawatt. With the non-linear effects of the non-uniform magnetic field in the spectrometer, the deconvolution of the energy spectrum from the IP images requires a good estimate of the point spread functions of the spectrometer, which are energy dependent. In addition, large backgrounds, especially in the low energy regime require careful subtraction to extract the data without losing the low energy signal. Once these aspects of the data have been determined, the data can then be deconvolved using a response matrix of the system for some input energy spectra and minimizing the produced position against the position data.

### 4.1 Background Profile

The first step in determining the energy spectrum of the electron and positron signal is the removal of the background signal. The background signal is determined to be a result of several different processes. Foremost, there is a nearly constant background that results from external gamma rays striking the case and the image plate. The internal background is a result of electron bremsstrahlung, secondary photoelectrons, scattered gamma rays from the pinhole, and electron reflux to the Fe yoke. The extreme background on the lowest energy portion of the image plates is due to the Fe yoke fluorescence. The lowest energy electrons are bent into the iron yoke by the magnetic field and in turn generate x-rays and secondary electrons. A lesser background is due to the electrons striking the magnets. To remove this background signal, the background is chosen to be the average of the signal inside the cavity above and below the electron signal. As can be seen in Figure 4.1, the defined background offers reasonable agreement with the electron signal. Unfortunately, simulation indicates that the lowest energy point spread functions have a large vertical spread. This would indicate that our method for background subtraction will remove some of the lowest energy electrons. Regardless, this method seems more accurate than removing only the background as seen in the magnet region (pink area), which is background mainly due to external radiation.

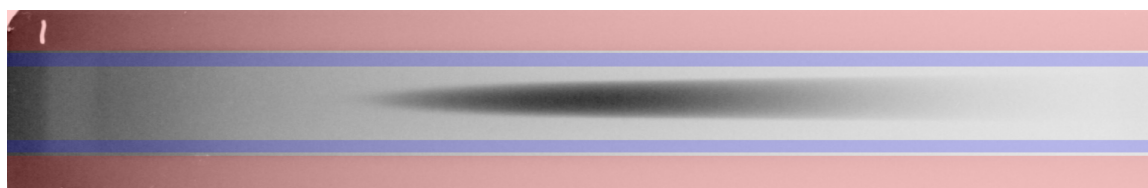


Figure 4.1: A schematic of the background profile. The pink regions are the magnets and are excluded. The blue regions are the spaces in the cavity between the signal and the magnets that are used to create the background profile. The background is taken as an average of the top and bottom of the cavity between magnets (blue lines).

### 4.2 Image Deconvolution

With the background removed from the image plate, we must now vertically integrate the data to get a position spectrum. From this spectrum, we wish to extract the energy spectrum. To do this, we must first construct a response matrix for the system. The response matrix is constructed from point spread functions generated from data from a simulated spectrometer constructed using the

GEANT4 Monte Carlo code. The Monte Carlo simulation was modeled by graduate student Henderson. The point spread functions are created in 0.1 MeV increments to allow for fine energy deconvolution. Sample PSF's are displayed in Figure 4.2. The energy-position spectrum is well matched to the calibration points gathered from the LSU electron LINAC beam lines [8] and a  $^{90}\text{Sr}$  source.

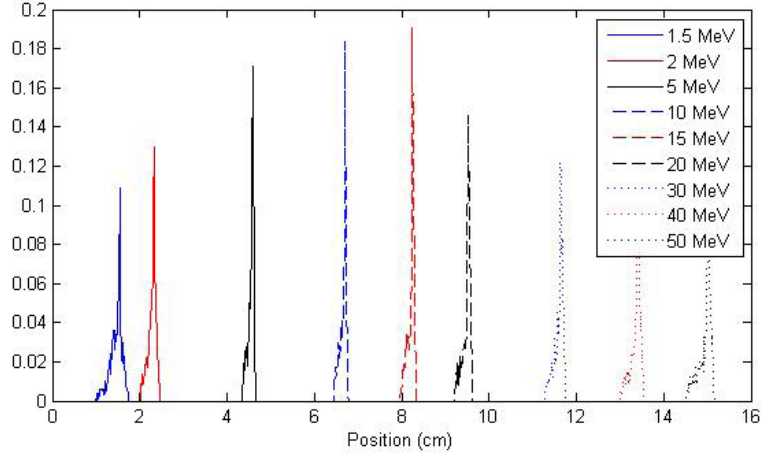


Figure 4.2: A view of several point spread functions generated from the output data of the GEANT4 Monte Carlo code.

Using the response matrix, we can now deconvolve the shot data. The deconvolution is non-trivial since we have to solve a large matrix equation of the form  $\mathbf{Ax} = \mathbf{b}$

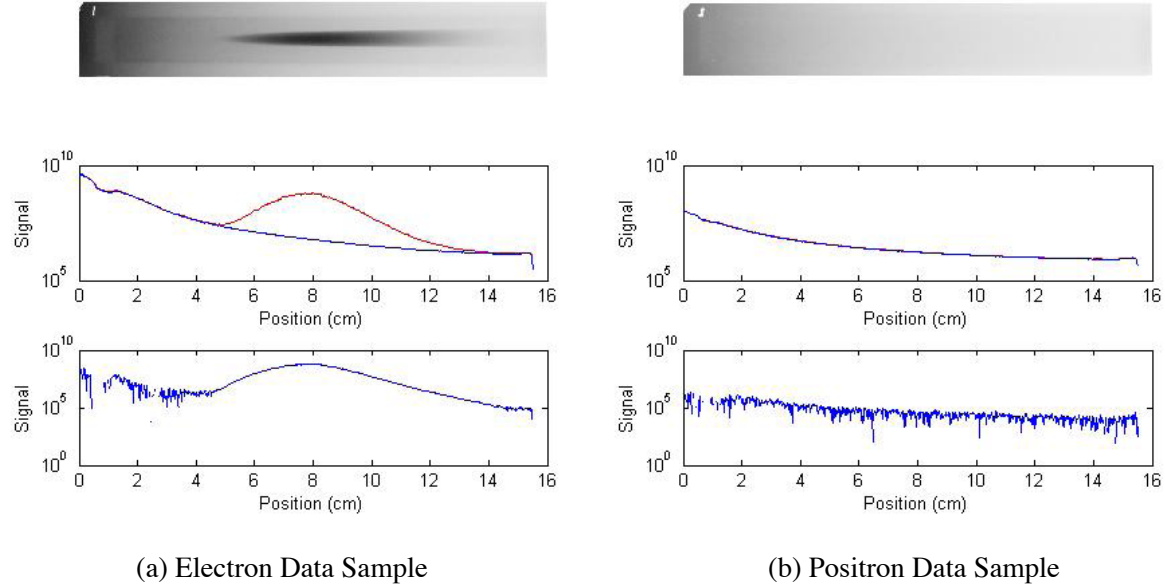


Figure 4.3: Example of background reduction for a 1 mm shot. The shot data is summed vertically (red line) and the data in the region between the signal and the magnets is taken to be the background (blue line). When no peak is visible, the resultant signal is taken to be the upper limit.

where  $\mathbf{A}$  is our response matrix,  $\mathbf{x}$  is the unknown energy spectrum, and  $\mathbf{b}$  is the position spectrum. Simply inverting the matrix may not produce desirable or smooth results since the problem is not well posed. It is therefore necessary to verify the inverted matrix spectrum by performing a minimization routine. The minimization routine is used to improve and optimize the solution of  $\|\mathbf{Ax} - \mathbf{b}\|^2 = 0$ .

Taking the position spectrum, and using the Monte Carlo generated response matrix, we are able to convert the data from position space to energy space. The deconvolved spectrum can be formulated in discrete energy bins. For analysis, 1MeV energy bins are chosen. The error is taken to be the standard deviation of the position spectrum from the IP data. While we are able to estimate the error in the position spectrum by looking at the random variation around the data, the response matrix's error is harder to estimate. There is error in the measurement of the magnetic field for the Monte Carlo simulation. However, accounting for this error by examining its effect on the response matrix output would prove too resource intensive to calculate. Instead, to estimate the error in the final energy spectrum, the input position spectrum is varied in a normal random distribution based on the standard deviation of the data (which is taken to be the error in the position spectrum data). We can then pass this position spectrum through the response matrix many times to estimate an error for the energy spectrum based on the error from the position spectrum. Thus we are left with an energy spectrum with appropriate errors as in Figure 4.4.

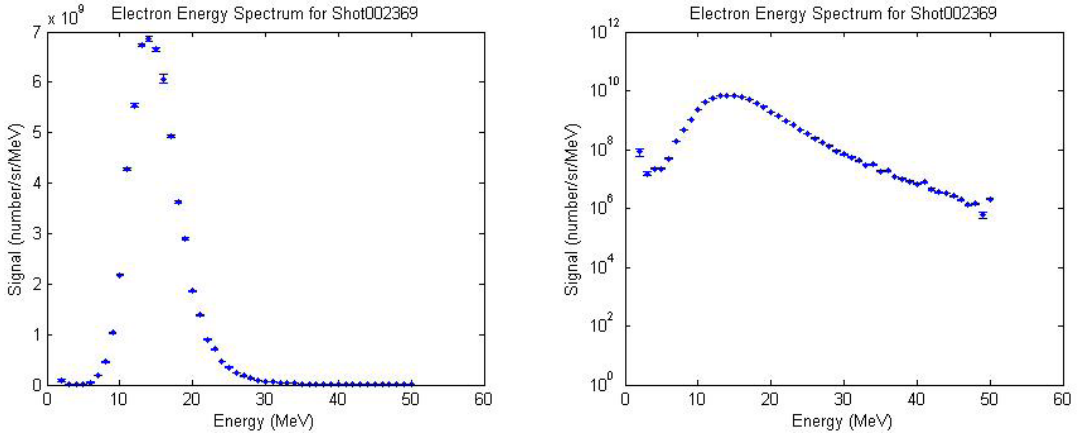


Figure 4.4: A sample deconvolved spectrum from the data presented in Figure 4.3a. The deconvolution is done in 1 MeV bins. Left is the spectrum in linear-linear plot. Right is the same spectrum in log-linear plot showing the exponential tail.

#### 4.3 Peak Energy and Effective kT

With the deconvolved data, we can now extract the peak energy of each shot as well as the effective kT. We then wish to understand the correlation between these values and incident laser intensity. Peak energy can be extracted by fitting the deconvolved data to a Gaussian curve and finding the energy of maximum value of this Gaussian. The effective kT is extracted by fitting the high energy tails of the deconvolved spectrum to an equation of the form  $N \sim \exp(-E/kT)$  where  $N$  is the signal and  $E$  is energy. An example of this fitting mechanism can be seen in Figure 4.5.

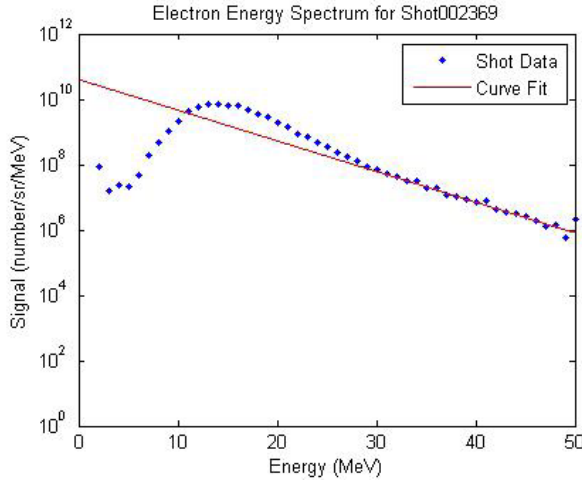


Figure 4.5: Sample exponential fit to extract effective kT.

## Chapter 5 Results

After running the analysis, it is determined that we were not able to see a convincing positron signal above the background. This is not unexpected since the laser intensity was below  $10^{20}\text{W/cm}^2$  and the x-ray background was high at low energies. However, we were able to extract useful and interesting electron data from our Au target shots. From the data we can compare peak energy and effective kT and their relation to incident laser intensity as noted in Figure 5.1. In addition, we now have a means of extracting energy spectra for future experimental runs. Note: the data points corresponding to shot 2365 have been neglected from analysis because of a clear alignment issue when examining the raw data.

In examining the energy spectra, the most surprising feature is the lack of low-energy electrons and narrowness of the electron peaks (see Figure 4.4). Previous experiments carried out at other lasers such as Titan, Vulcan and Omega EP, as well as our own Monte Carlo simulations have found broader electron peaks with more low energy electrons. This dearth of low energy electrons is curious and could be indicative that the hot electrons may be accelerated by other mechanisms besides ponderomotive acceleration, such as accelerations in the pre-plasma that produce narrow band electrons. The results remain to be confirmed in future Texas Petawatt experiments. While there does appear to be a good correlation between laser intensity, effective kT, and peak energy (Fig.5.1), there is one anomalous data point. This may be attributed to an error in the reporting of the peak intensity on target. The data point is marked with a red square in Figure 5.1 and corresponds to shot 2357. Analysis of this data would indicate that the intensity must be greater than that reported. Ignoring this data point, we do see a positive trend between intensity and peak energy in Figure 5.1a and a positive trend between intensity and effective kT in Figure 5.1b. Finally, in Figure 5.1c, where we directly compare effective kT and peak energy, we see a good correlation even including this anomalous data point.

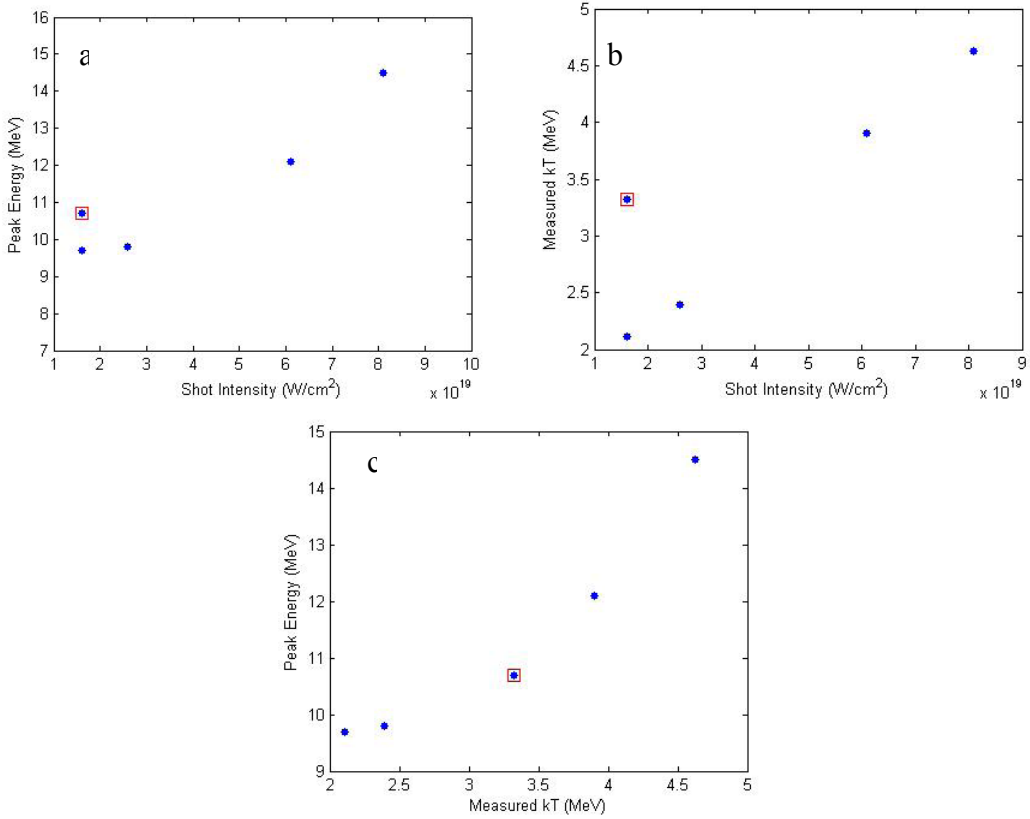


Figure 5.1: The correlations between measured shot intensity, peak energy, and effective temperature  $kT$  for 1mm Au targets irradiated by the TPW.

When we plot the 4 data points without the stray point on a log-log plot (Fig.5.2), we see that the effective temperature  $kT$  scales with laser intensity as a power law of index  $\sim 1/2$ . This is consistent with ponderomotive scaling. To first order, the peak electron energy also scales with laser intensity as a power law of index of  $\sim 1/4$ . But the trend suggests that it may be steeper than a power law. More data is needed to confirm this and the physics for such a trend remains to be understood. Finally we see that the correlation between peak energy and  $kT$  is steeper than a power law, even though a power law of index  $\sim 0.5$  is also a rough fit to first order.

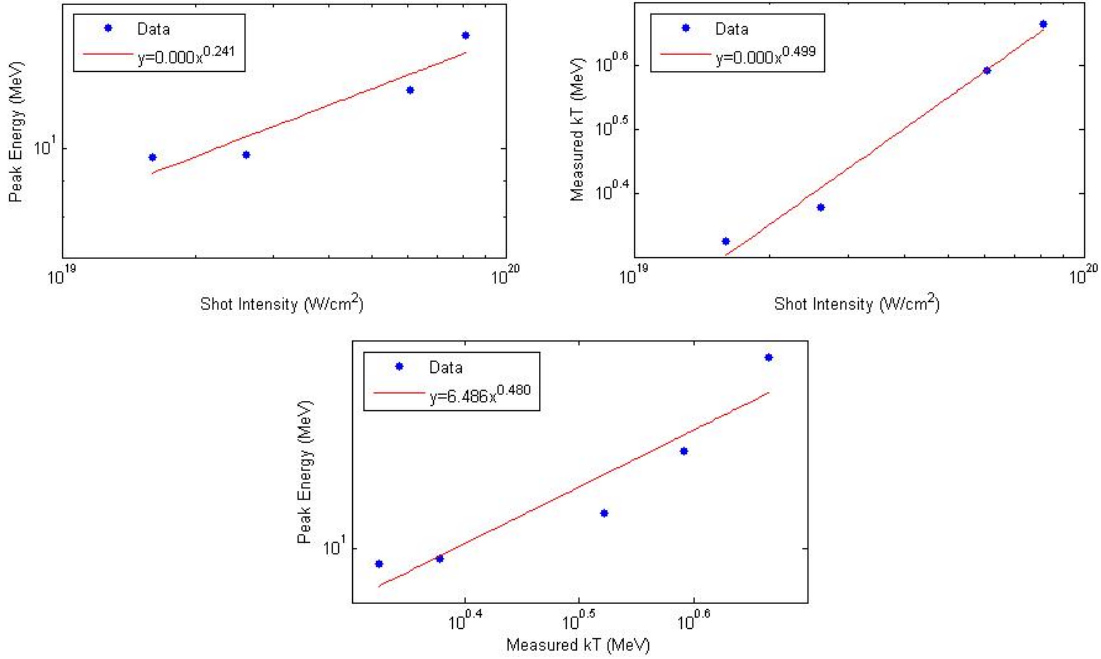


Fig.5.2 Same as Fig.5.1 in log-log scales.

## Chapter 6 Discussion and Future Work

The lack of any clear positron signal could be due to a combination of several factors: (a) our laser energy per shot is only  $\sim 50$  J. This is much lower than the Titan and Omega-EP shots by Chen et al [3]. (b) Lower laser energy means fewer hot electrons and lower sheath electric field, which renders any emergent positron to have too low an energy to be observed above the background. (c) Our shielding may be insufficient to reduce the background to the level of the Titan and Omega-EP shots. Future TPW experiments should improve on all of these.

The deficit of low energy electrons in our data makes the electron distribution resemble a quasi-mono-energetic beam. This may be caused by the unique properties of the TPW laser. If confirmed by future experiments, this bodes well for potential applications of such electron beams such as in medical therapy. The physics reasons underlying such a narrow electron peak remains to be investigated and explained.

The next stage of this project has already begun. For the summer of 2012, we have scheduled a 5-week run at the Texas Petawatt laser. The laser has recently undergone an upgrade to reach a maximum energy of 180 J. In addition, the time compression of the laser has been improved to allow a consistent pulse duration of 170 fs or less. From this we can expect a maximum laser intensity on target of approximately few  $\times 10^{21}$  W/cm<sup>2</sup>, making this the most intense high-energy petawatt class laser in the world.

### Acknowledgement

This work was supported by the DOE grant DE-SC-000-1481.

## Appendix A

### Table of Shot Parameters

| Shot Number | Target | Position | Image Plate Fade Time | Peak Laser Intensity        |
|-------------|--------|----------|-----------------------|-----------------------------|
| 2336        | 3mm Au | 20em     | 32 min                | $7.0 \times 10^{19} W/cm^2$ |
| 2340        | 3mm Al | 20em     | 29 min                | $2.5 \times 10^{19} W/cm^2$ |
| 2341        | 3mm Au | 29em     | 32 min                | $2.1 \times 10^{19} W/cm^2$ |
| 2342        | 3mm Au | 29em     | 34 min                | $4.3 \times 10^{19} W/cm^2$ |
| 2349        | 2mm Au | 18em     | 28 min                | 100TW*                      |
| 2353        | 2mm Au | 18em     | 44 min                | $2.4 \times 10^{19} W/cm^2$ |
| 2354        | 4mm Au | 16em     | 25 min                | 200TW*                      |
| 2356        | 2mm Au | 16em     | 20 min                | 177TW*                      |
| 2357        | 1mm Au | 16em     | 23 min                | $1.6 \times 10^{19} W/cm^2$ |
| 2364        | 1mm Au | 16em     | 19 min                | $6.1 \times 10^{19} W/cm^2$ |
| 2365        | 1mm Au | 16em     | 21 min                | $1.4 \times 10^{19} W/cm^2$ |
| 2366        | 1mm Au | 16em     | 20 min                | $1.6 \times 10^{19} W/cm^2$ |
| 2368        | 1mm Au | 16em     | 18 min                | $2.6 \times 10^{19} W/cm^2$ |
| 2369        | 1mm Au | 16em     | 16 min                | $8.1 \times 10^{19} W/cm^2$ |

\*Farfield of laser off screen, approximate measurement of intensity not possible.

Table A.1: Target and spectrometer properties for each shot as well as observed intensity data.

### References

- [1] Edison Liang et al. “Pair production by ultraintense lasers”. Phys. Rev. Lett., 81, 1998.
- [2] Hui Chen et al. “Absolute calibration of image plates for electrons at energy between 100 keV and 4 MeV”. Rev. Sci. Instrum., 79(033301), 2008.
- [3] Hui Chen et al. “Relativistic positron creation using ultraintense short pulse lasers.” Phys. Rev. Lett., 102(105001), 2009.
- [4] J. O. Deasy et al. “Measured electron energy and angular distributions from clinical accelerators”. Med. Phys., 23, 1996.
- [5] Kazuo A. Tanaka et al. “Calibration of imaging plate for high energy electron spectrometer”. Rev. Sci. Instrum., 76(013507), 2005.
- [6] Mikael Martinez et all. “The texas petawatt laser”. Proc. of SPIE, 5991(59911N-1), 2005.
- [7] Edison Liang “Intense laser pair creation and applications”. High Energy Density Physics, 6:219-222, 2010.
- [8] Kenneth Hogstrom et al. “Measurement of Elekta Electron Energy Spectra Using a Small Magnetic Spectrometer”, AAPM Conf. Abstract 2012.
- [9] Scott Wilks, et al. Phys. Rev. Lett. 69, 1383, 1992.
- [10] W. Heitler *Quantum Theory of Radiation* (Oxford, UK), 1954